



Transient absorption spectroscopy and imaging of redox in muscle mitochondria

ERKANG WANG,¹ LUKE A. WHITCOMB,² ADAM J. CHICCO,² AND
JESSE W. WILSON^{1,3,*} 

¹Department of Electrical & Computer Engineering, Colorado State University, 1373 Campus Delivery, Fort Collins, CO 80523, USA

²Department of Biomedical Sciences, Colorado State University, 1601 Campus Delivery, Fort Collins, CO 80523, USA

³School of Biomedical Engineering, Colorado State University, 1301 Campus Delivery, Fort Collins, CO 80523, USA

*jesse.wilson@colostate.edu

Abstract: Mitochondrial redox is an important indicator of cell metabolism and health, with implications in cancer, diabetes, aging, neurodegenerative diseases, and mitochondrial disease. The most common method to observe redox of individual cells and mitochondria is through fluorescence of NADH and FAD⁺, endogenous cofactors serve as electron transport inputs to the mitochondrial respiratory chain. Yet this leaves out redox within the respiratory chain itself. To a degree, the missing information can be filled in by exogenous fluorophores, but at the risk of disturbed mitochondrial permeability and respiration. Here we show that variations in respiratory chain redox can be detected up by visible-wavelength transient absorption microscopy (TAM). In TAM, the selection of pump and probe wavelengths can provide multiphoton imaging contrast between non-fluorescent molecules. Here, we applied TAM with a pump at 520nm and probe at 450nm, 490nm, and 620nm to elicit redox contrast from mitochondrial respiratory chain heme proteins. Experiments were performed with reduced and oxidized preparations of isolated mitochondria and whole muscle fibers, using mitochondrial fuels (malate, pyruvate, and succinate) to set up physiologically relevant oxidation levels. TAM images of muscle fibers were analyzed with multivariate curve resolution (MCR), revealing that the response at 620nm probe provides the best redox contrast and the most consistent response between whole cells and isolated mitochondria.

© 2022 Optica Publishing Group under the terms of the [Optica Open Access Publishing Agreement](#)

1. Introduction and background

The most widely used methods to measure mitochondrial functions are based on fluorescence, either by autofluorescence of endogenous fluorophores NADH/FAD⁺ [1] or extrinsic fluorescence labeling [2]. NADH and FAD⁺ are fluorescent cofactors that deliver high-potential electrons as input to the respiratory chain. From there, a sequence of non-fluorescent heme proteins (cytochromes) mediate electron transport, converting their potential energy into an electrochemical gradient across the inner mitochondrial membrane. Finally, this electrochemical gradient drives the production of ATP. Exogenous labels such as mitotracker and photochromic fluorescence resonance energy transfer (pcFRET) [2]. can probe redox within the respiratory chain and its output membrane potential. However, extrinsic labels can perturb the natural mitochondrial metabolism [2] and it is also hard to label small protein molecules such as cytochromes. Developing a label-free approach to microscopic redox imaging of the respiratory chain remains an active area of research, in spite of the fact that, like most porphyrins, these heme proteins exhibit clear redox-sensitive absorption spectra.

To date, label-free approaches to respiratory chain redox microscopy have used Raman [3–6], photothermal [7], and photoacoustic [8] effects for imaging contrast. Even though the underlying

Raman vibrational modes and optical absorption peaks are distinct for redox states of the respiratory hemeproteins, these methods have yet to show contrast for normal physiological changes in mitochondrial redox, instead relying on extreme preparations to manipulate redox, such as the addition of respiratory chain poisons. In this paper, we use transient absorption microscopy (TAM) [9,10] at several different probe wavelengths to see whether picosecond-timescale excited-state relaxation in hemeproteins is sensitive to mitochondrial respiratory chain redox in the absence or presence of natural mitochondrial fuels (malate, pyruvate, and succinate).

The ultrafast dynamics of isolated hemeproteins have been frequently studied by means of transient absorption spectroscopy (TAS), in which an optical probe pulse measures changes in absorption after excitation by a pump pulse [11]. From this, the following processes have been observed [12–16]. Excitation promotes the π electrons of the porphyrin ring to an electronic excited state, followed by rapid ligand-to-metal charge transfer. In the reduced (Fe^{2+}) state, this breaks the bond between the metal ion and the axial ligand (a methionine residue in the case of electron transport cytochromes, or O_2 , CO, or NO in the case of oxygen transport/catalysis hemes such as hemoglobin, myoglobin, and cytochrome *a3*). This is followed by rapid relaxation to a vibrationally hot ground state, reattachment of the axial ligand, and vibrational cooling. The exact processes and relaxation time constants observed depend on the hemeprotein structure, charge state, the axial ligand, and the pump/probe wavelengths involved [14]. This dependence enables TAS to distinguish between different hemeproteins, oxidation, or ligand states with an appropriate selection of pump and probe wavelengths. Thus, transient absorption imaging, i.e. TAM, has been used to distinguish hemoglobin from its glycated form found in diabetics [17], oxy- versus deoxy-hemoglobin [18–20], hemoglobin versus hemozoin in plasmodium (malaria)-infected red blood cells [21], and to track heme storage and transport in *C. elegans* [22].

Previously, we reported spectroscopy of cytochrome *c* and label-free TAM imaging of cryosectioned tissue at 530nm pump (an absorption peak of oxidized, Fe^{3+} , cytochrome *c*) and 490nm probe (a low-absorption wavelength in between the Soret band and Q-band of the cytochromes) with a homebuilt fiber laser source, in addition to TAS of respiratory chain supercomplexes showing excited-state lifetime differences corresponding to mitochondrial disease [23,24]. Here, we move to a commercial two-color ultrafast source (Insight X3, SpectraPhysics), and frequency-double the fundamental (1040nm) to produce a 520nm pump (an absorption peak of reduced, Fe^{2+} cytochrome *c*). With the tunable output of the X3, we frequency-double to produce a probe at 450nm, 490nm, and 620nm. These are selected to maximize contrast by considering the TA response of cytochrome *c* (see Figs. 2(b,d) in [13]): 450nm results in a signal that is of opposite sign for reduced (ground state bleach) and oxidized (excited-state / hot band absorption); 620nm results in a cyt *c* signal that is significantly larger than that at 450nm or 490nm, for the oxidized state and has a more pronounced lifetime difference between reduced and oxidized states. This is of course, an approximate starting point, as the TA response of mitochondria will need to consider all of the respiratory chain hemeproteins and account for the likelihood that the TA responses of these hemeproteins will be different in isolation versus in their native molecular environment within the inner mitochondrial membrane. TAM imaging experiments were conducted on fresh reduced and oxidized muscle fiber preparations. The reduced preparations are achieved by the addition of mitochondrial fuels to oxidized mitochondria. We find that the picosecond-timescale change in probe absorptivity after pumping shows an excited state lifetime difference between two mitochondrial redox states. Applying multivariate curve resolution (MCR) to muscle tissues' TA image stacks reveals pixel-wise lifetime difference among mitochondria within muscle fibers, and the strongest redox contrast coming from a 620nm probe. The realization of TA images from live tissue with hemeprotein redox contrast takes us one step closer to applications, for example, in cancer metabolism and noninvasive evaluation of mitochondrial diseases.

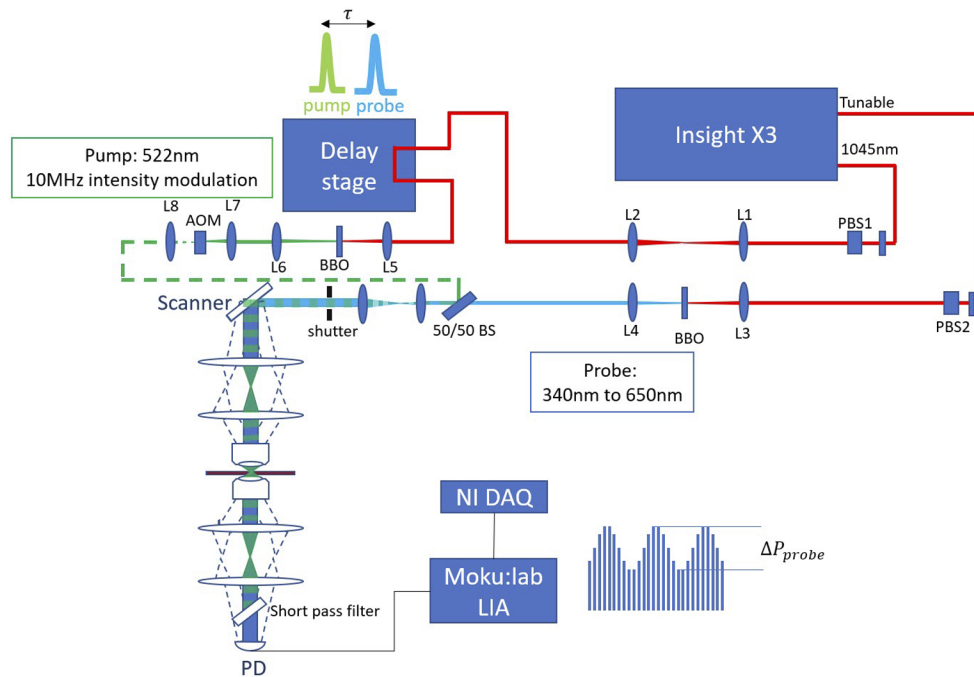


Fig. 1. Experimental setup. Both arms of the laser source (Insight X3) pass through a polarizing beamsplitter (PBS) for variable attenuation. The pump arm (1045 nm) is routed through a motorized delay stage. Both arms are frequency-doubled in β -barium borate (BBO), and the pump arm is modulated by an AOM. Visible-wavelength pump (522 nm) and probe (tunable 340 to 650 nm) are combined in a beamsplitter (BS) and directed into a laser-scanning microscope. Transmitted probe is collected by a photodiode (PD) and analyzed with a lock-in amplifier (LIA).

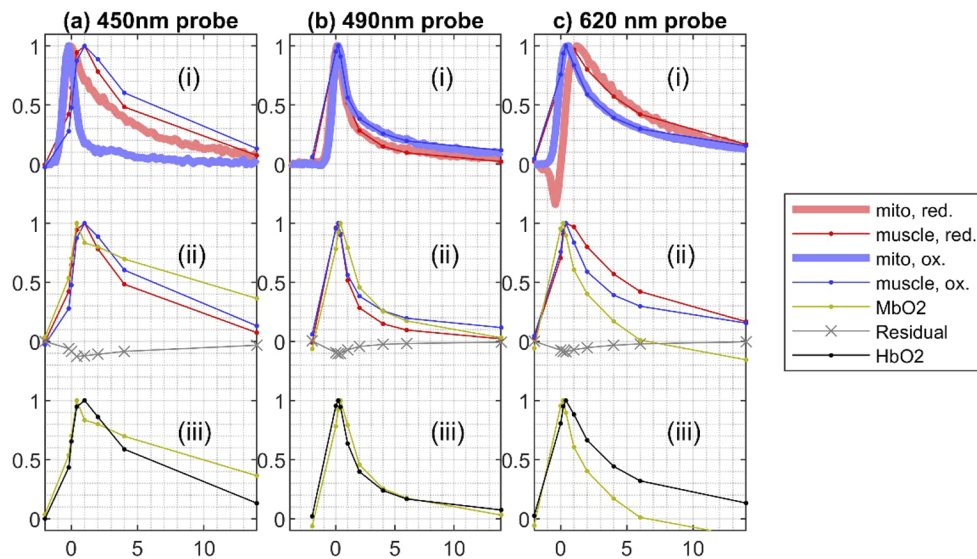


Fig. 2. Transient absorption response curves. Solid lines indicate measurements on isolated mitochondria; thin lines extracted from muscle fiber imaging. See text for details.

2. Methods

2.1. Experimental setup

Our TAM imaging system (Fig. 1) is based on an Insight X3 ultrafast laser source (80 MHz repetition rate, ~ 100 fs pulse width), with each output frequency-doubled in a BBO crystal (0.5mm thickness, Type I phase matching, EKSPA BBO-651H) to provide a visible-wavelength pump/probe pulse pair. The fixed 1045 nm output is frequency doubled to produce a 522 nm pump beam. The tunable (680nm—1300nm) output is frequency doubled to produce a visible probe beam tunable from 340 nm to 650 nm. After frequency doubling, the 522 nm pump beam and the tunable visible probe beam are combined by a 50/50 beam splitter (used instead of a dichroic because the tunable probe arm can be of longer or shorter wavelength than the 522nm pump). The two collinear beams are then expanded from 1mm diameter to 10mm diameter through a telescope and directed to a home-built laser scanning microscope (LSM).

Our previous results with a stage-scanning LSM were limited by heat buildup at the focal spot, which spoiled the lifetime contrast between reduced and oxidized hemeproteins [23]. From a thermal transport model, we estimated that the focused laser beams need to be scanned on order of 1 m/s to limit heating to a few Kelvin at the focal spot [25]. Therefore, we constructed a LSM with a 3.5 kHz resonant scanner along the x axis and a 2.5 Hz rate along the y axis, achieving a 3m/s velocity over a $425\mu\text{m}$ line. A 4- f system right after the scanner then conjugates the scanner plane to the back aperture of the objective lens (Olympus UPlanFL N 20X/0.50). Then the collinear scanning pump and probe beams are focused onto the sample, resulting in a scan pattern covering a $425\mu\text{m} \times 700\mu\text{m}$ field of view (FOV). Transmitted light is collected by a condenser lens (Nikon Plan APO 20X/0.75). Lastly, a pump-rejecting filter (FES0500 Thorlabs) only allows the probe to pass through and another 4- f system relays the back aperture of the condenser lens to a photodetector (PD). The high numerical aperture of the condenser and the second 4- f system, which shrinks the probe beam diameter to the size of the PD's active area, mitigate photothermal lensing on the probe.

The difference of arrival time τ into the sample between spatially overlapped pump and probe beams is controlled by a motorized delay stage. The pump laser pulse train is intensity modulated at 10 MHz by an acoustic optical modulator (AOM, TEM-100-25, Brimrose). This frequency is selected to ensure several on/off pump modulation cycles per pixel (the 3.5 kHz line rate, at 516-pixels per line, results in a pixel dwell time of 277 ns). Detection consists of a photodetector (Thorlabs SM05PD1B), a 50 Ω pass through terminator, a 1MHz high pass filter, a 20MHz low pass filter and a low noise pre-amplifier (Edmund Optics 59-179). The combination of the high pass and low pass filter not only blocks the large DC component, but also limits the aliasing outside 1MHz to 20MHz. Finally, the pump-induced changes in probe transmissivity $\Delta P_{\text{pr}}(\tau)$ are then detected with a lock-in amplifier (LIA, Moku:lab) with the output low-pass filter set to a 1 MHz, 24 dB/octave cutoff.

At each τ , we acquire TA image data with the scanning LSM for 5 seconds, equivalent to 10 frames. A shutter blocks the beam in between acquisitions to minimize exposure to light when changing τ . The data acquisition device (DAQ, NI PXI-6133 records simultaneously the scanner x position, y position, and the LIA in-phase output (which is proportional to $\Delta P_{\text{pr}}(\tau)$). Pump-probe signal levels over the scan region were compared before and after each stack; any image stacks with a noticeable drop (either from photobleaching of the hemes or from z -drift of the sample) were discarded. For each 10-second acquisition, the time-domain data was then reconstructed into an image with isotropic $1\mu\text{m}^2$ pixels with `gridfit()`, a regularized grid fitting function [26]. The phase shift between the x position and the acquired signal was fine-tuned by applying linear spectral phase to the acquired signal, adjusting the slope to maximize standard deviation of the reconstructed images (during this adjustment, `gridbin()` was used to speed up reconstruction [27]; final reconstruction was done with `gridfit()`).

Laser power used was 24mW for the 522nm pump, 17mW for the 450nm probe, 53mW for the 490nm probe, and 24.5mW for the 620nm probe. Except for 450nm, which was attenuated to prevent photobleaching, these were set to the maximum available out of the frequency-doubling stages. While further study is needed to understand the impact of ultrafast pulses on cell damage, we note that a recent detailed study on damage in LSM with ultrafast 1040nm pulses by Talone, et al. [28] found phototoxicity to be dependent on average power P , number of lines L scanned over a $2500 \mu\text{m}^2$ area, and scanning speed V_s , where $x = P[W] \times L \times V_s[\text{mm/s}]^{-0.08} < 5.367$ resulted in minimal photodamage (<5% probability of cell death). Adjusting this for the larger area over which the laser exposure is spread out in our scenario, 0.2975 mm^2 , a factor of 119 larger, results in $x' = x \times (2500 \mu\text{m}^2) / \text{FOV} = x/119$. For the delay stacks, with 5 sec acquisition time and a 3.5 kHz line rate, $L = 35,000$. Our worst-case scenario (77 mW total power) is then $x = 1 \times 10^{-3}$, three orders of magnitude within Talone's $\lambda = 1040\text{nm}$ safety limit. However, this rule of thumb does not account for increased absorption and heating of hemeproteins at shorter wavelengths. For example, we noted that at 450nm probe, $>17\text{mW}$ ($x = 1.8 \times 10^{-3}$) caused photobleaching of the TA signal (hemeproteins absorb significantly more energy at 450nm due to the strong Soret band, thus increasing local heating). Clearly, further studies are needed on ultrafast pulse phototoxicity to discover the wavelength dependence of the phototoxicity parameter x .

2.2. Sample preparation

Samples were prepared from skeletal muscles of adult (6-8 month old) C57Bl/6N mice (Jackson Labs, Bar Harbor, ME) housed in a temperature-controlled facility with water and food provided *ad libitum*. Animals were sacrificed by carbon dioxide inhalation followed by midline thoracotomy and removal of the heart using procedures approved by the Colorado State University Care and Use Committee in accordance with the Guide for the Care and Use of Laboratory Animals published by the U.S. National Institutes of Health [29]. Hindlimb muscle tissues were immediately harvested for preparation of isolated mitochondria, permeabilized muscle fibers, or intact muscle tissue. Mitochondria were isolated from homogenized sections of gastrocnemius, plantaris and tibialis anterior muscles using differential centrifugation methods previously described in detail [30]. Soleus muscles from the same animals were carefully removed intact and placed in ice-cold BIOPS preservation solution containing (in mM) 0.1 μM free calcium, 20 imidazole, 20 taurine, 50 K-MES, 0.5 DTT, 6.56 MgCl_2 , 5.77 ATP, 15 phosphocreatine, pH 7.1. One soleus muscle ($\sim 10 \text{ mg}$) was teased with sharp forceps into fiber bundles and incubated with 50 $\mu\text{g/ml}$ saponin in BIOPS on ice for 20 minutes with gentle rocking to permeabilize cell membranes and remove myoglobin while leaving mitochondrial membranes intact [30,31]. The contralateral soleus was left intact in ice-cold BIOPS until analysis.

To generate reduced and oxidized preparations, samples were transferred to mitochondrial respiration medium (MiR05; [30]) and incubated at 37°C for 5-10 minutes with (reduced) or without (oxidized) mitochondrial substrates (1 mM malate, 5 mM pyruvate, 20 mM succinate) in the absence of adenosine diphosphate. This protocol provides saturating levels of reducing equivalents to the respiratory chain through Complexes I and II (reduced), or depletes any endogenous substrates present in the sample in the absence of exogenous substrates (oxidized).

3. Results and discussion

3.1. Mitochondrial redox spectroscopy

TA spectroscopy of isolated mitochondria in suspension was performed with the LIA time constant set to 0.1sec, stepping τ from -2ps to 16ps in 0.2ps increments, while the imaging scan mirrors are running to prevent heating at the focus. The resultant delay scans are shown as thick solid lines in Figs. 2(a)(i), 2(b)(i), and 2(c)(i). For 490nm probe, oxidized versus reduced mitochondria have a longer lifetime, while both 620nm and 450nm probe reveal oxidized mitochondria to

have shorter lifetimes. 450nm probe reveals the strongest redox contrast, while 490nm shows the smallest difference between redox states. These can be compared with the averaged signals from muscle fibers (red and blue thin dot lines), HbO_2 response and the MCR-estimated MbO_2 response (yellow and black thin dot lines), as discussed below.

3.2. Muscle fiber imaging

TAM delay stacks of muscle fibers were then acquired with $\tau = \{-2\text{ps}, 0\text{ps}, 0.2\text{ps}, 0.4\text{ps}, 1\text{ps}, 2\text{ps}, 4\text{ps}, 6\text{ps} \text{ and } 14\text{ps}\}$. An example TAM delay stack of permeabilized muscle fibers with 522nm pump / 620nm probe is shown below in Fig. 3. The absence of signal at $\tau = -2$ ps indicates the absence of any appreciable photothermal or long-lived (ms to μs timescale) signals. A sharp rise in ΔP_{pr} is seen at $\tau = 0\text{ps}$, which decays almost entirely within 14ps. This image shows a striated pattern inside the fibers and bright spots distributed along the periphery of the fibers. These striations and bright spots are consistent with intra-fibrillar mitochondria (IFM) and paravascular mitochondria (PVM), respectively, typically observed in fluorescent staining of mitochondria in muscle fibers (see, e.g. Figure 4 of Ref. [32]). Besides the striated structures, we can still observe a faint background inside each cell. This background may be from myoglobin, other heme proteins, and out-of-focus mitochondria. Myoglobin is diffused throughout the cytoplasm and has $8\text{--}10\text{mM}^{-1}\times\text{cm}^{-1}$ molar absorptivity at 522 nm [33], compared with $16\text{mM}^{-1}\times\text{cm}^{-1}$ for reduced cytochrome *c* [14]. Considering that both myoglobin and cytochrome *c* have about 0.5 mM concentrations in cytoplasm and mitochondria, respectively, and that cytochrome *c* is just one of four mitochondrial heme proteins that can contribute signal, the mitochondrial contribution to the measured TA signal is expected to have a two- to eight-fold stronger signal than myoglobin. The bright spots of $\sim 5\mu\text{m}$ diameter on the periphery of the muscle fibers are likely red blood

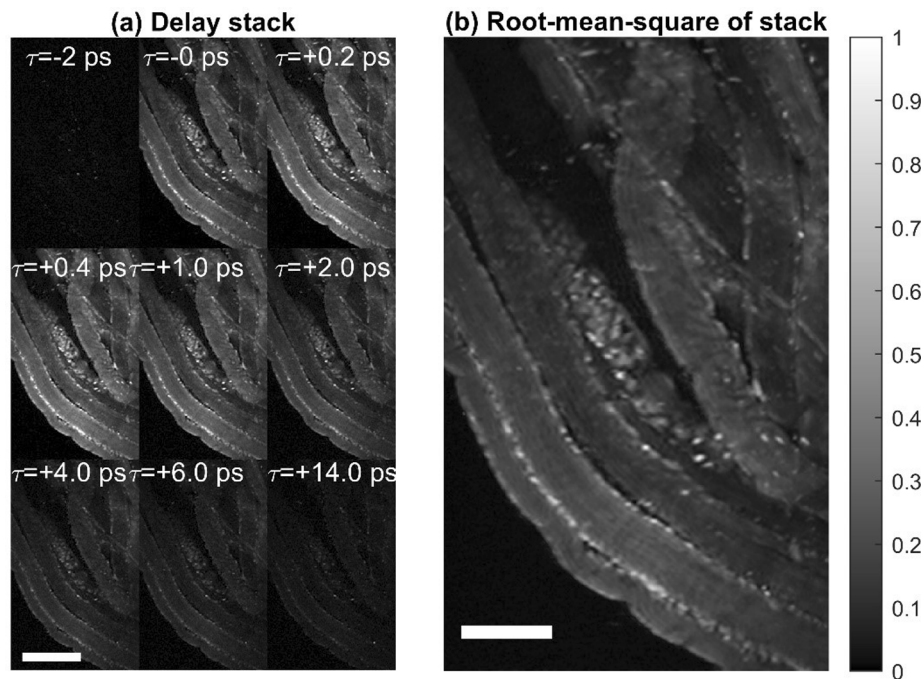


Fig. 3. Transient absorption imaging stack, 620 nm probe. 100 μm scale bar. (a) Frames acquired at different probe delay times. (b) Root-mean-square taken across all probe delay times.

cells, considering their diameter, and that each hemoglobin molecule contains four heme groups, and thus a $4\times$ stronger absorption cross-section than mitochondrial cytochromes or myoglobin.

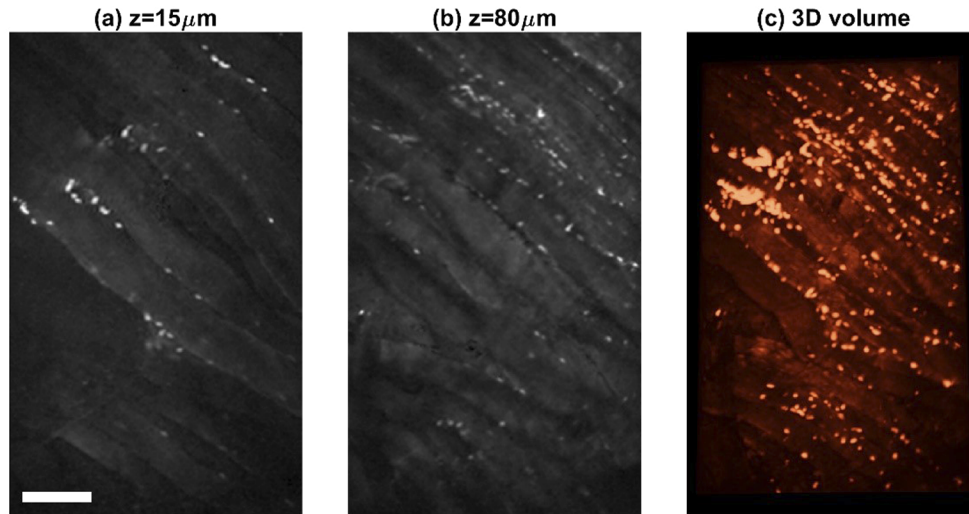


Fig. 4. Z-stack of muscle fibers at $\tau = 0$ ps probe delay. (a) Slice at $z = 15 \mu\text{m}$, (b) slice at $z = 80 \mu\text{m}$, and (c) maximum intensity projection rendering of entire stack. Scale bar $100 \mu\text{m}$. See also [Visualization 1](#).

Transient absorption is a two-photon process, and like two-photon fluorescence microscopy, is capable of intrinsic optical sectioning. To demonstrate this with visible-wavelength TAM, we acquired a 3D volume of reduced intact muscle fibers at 490 nm probe, setting the pump-probe delay to $\tau = 0$ ps and stepped through the sample stage (ASI) along z axis for $100 \mu\text{m}$ with a step size of $2 \mu\text{m}$. At each z slice, 20 frames of images are acquired and averaged, then the whole stack is filtered with a 3×3 median filter before interpolation to a volume with $1 \mu\text{m}^3$ isotropic voxels. Representative z -slices and a volume rendering (maximum intensity projection, using MATLAB's built-in `volshow` function) are shown in Fig. 4. An animated, rotating volume rendering is provided in [Visualization 1](#). The thickness of the acquired volume suggests that visible-wavelength TAM has the potential for imaging not just cell cultures but tissues as well, though it should be noted our current configuration detects transmitted, rather than backscattered light.

3.3. Multivariate curve resolution (MCR) analysis of delay stacks

Transient absorption stacks were analyzed with multivariate curve resolution (MCR) [34,35] in order to retrieve the underlying signals corresponding to reduced and oxidized mitochondria and myoglobin and assign to each pixel an estimated redox ratio. In transient absorption imaging, this process of identifying the underlying components (i.e. spectral endmembers) is frequently done through principal component analysis (PCA) and phasor analysis [36]. Both PCA and phasor project the data onto an orthogonal basis. Because the transient absorption signals of the underlying components are often non-orthogonal (as can be seen from the reduced and oxidized responses of isolated mitochondria), additional steps are needed to identify the spectral endmembers [37]. Here we use MCR instead, which can recover non-orthogonal components with non-negative concentrations and has been successfully used to estimate underlying components and distributions in similar scenarios such as coherent Raman microscopy and transient absorption spectroscopy [24,38,39]. Here, MCR was set up as an alternating least-squares problem (MCR-ALS) with a non-negative concentrations constraint, two known components supplied by the

averaged reduced and oxidized responses from the interior regions of permeabilized muscle fibers, and a third unknown component to account for myoglobin.

In brief, MCR-ALS assumes the measured transient absorption responses \mathbf{Y} to be a linear mixture of some underlying basis \mathbf{X} plus some noise \mathbf{N} :

$$\mathbf{Y} = \mathbf{MX} + \mathbf{N}. \quad (1)$$

Here, \mathbf{Y} is an $(n_y \times n_x \times n_s) \times n_{tau}$ matrix with each row containing the transient absorption response of an image pixel. \mathbf{Y} is arranged to contain measurements from the mitochondrial portion (interior of the fibers), from all image stacks sharing a common probe wavelength. Each image stack is n_x pixels across, n_y pixels tall, n_τ probe delays deep, and there are n_s stacks. \mathbf{X} is the underlying $n_c \times n_\tau$ basis, where $n_c = 3$ is the number of components assumed. \mathbf{M} is the $(n_y \times n_x \times n_s) \times n_c$ mixing matrix, where each row contains the concentrations of the underlying components for a pixel. Specifically, the entries along the first column, $M_{i,1}$ represents the magnitude of the reduced component, $M_{i,2}$ represent the oxidized component, and $M_{i,3}$ represents the magnitude of the myoglobin component. The first two basis of the initial estimate $\hat{\mathbf{X}}$ is formed from the averaged signals of the interior of reduced and oxidized, permeabilized (lacking myoglobin) preparations of muscle fibers, respectively. The initial guess for myoglobin is provided by the average of the bright hemoglobin response of red blood cells at the periphery and between intact muscle fibers. Then an estimate of \mathbf{M} , that is, $\hat{\mathbf{M}}$, is formed by use of the Tikhonov-regularized [40] pseudo-inverse of $\hat{\mathbf{X}}$,

$$\hat{\mathbf{M}} = \mathbf{Y} \hat{\mathbf{X}}^+. \quad (2)$$

Next, the non-negativity constraint is applied by setting all negative elements of $\hat{\mathbf{M}}$ to zero. Then the estimate of $\hat{\mathbf{X}}$ is updated,

$$\hat{\mathbf{X}} = \hat{\mathbf{M}}^+ \mathbf{Y}. \quad (3)$$

Then the first two rows of $\hat{\mathbf{X}}$ are replaced with the known averaged TA signal of reduced and oxidized, permeabilized muscle fiber, the third row is allowed to change to account for the myoglobin response. This process of alternately estimating \mathbf{X} , \mathbf{M} , and enforcing the non-negativity and known components constraint is repeated until convergence. Then one final step estimating all three components of \mathbf{X} is performed without replacement of the first two rows.

The results of MCR-recovered components $\hat{\mathbf{X}}$ are shown in Figs. 2(a)(ii), (b)(ii), and (c)(ii) for 450nm, 490nm, and 620nm probe, respectively. Figures 2(a)(iii), (b)(iii), and (c)(iii) show the comparison between MCR recovered myoglobin versus the hemoglobin response estimated by thresholding the brightest pixels. Fitting residuals, normalized to stack peak signal are shown in thin gray lines. In all three cases, the MCR-recovered basis shows typical positive excited state absorption (ESA) responses and myoglobin lifetimes are different from reduced and oxidized muscle. Both 490nm and 620nm probe wavelengths revealed good agreement between isolated mitochondria and MCR-recovered components. In addition, when comparing reduced versus oxidized mitochondrial component, it can clearly be seen that 620nm probe offers the largest differences in excited-state lifetime.

Next, the MCR-recovered concentrations of each pixel are used to generate false-color images of each TAM stack. The reduced, oxidized, and myoglobin components are mapped to yellow, cyan, and magenta, respectively by setting the {red, green, blue} value of each pixel to $\{M_{i,1} + 3M_{i,3}, M_{i,1} + M_{i,2}, M_{i,2} + 3M_{i,3}\}$. The resulting images for 450nm, 490nm, and 620nm probe wavelengths are shown in Figs. 5, 6, and 7, respectively. As expected from the response curves in Fig. 2, the separation between reduced and oxidized muscle fiber preparations was poor for 450nm and 490nm, but clear at 620nm. The 620nm probe also reveals the clearest difference between intact and permeabilized muscle fibers, in terms of the third component (myoglobin), visible by the third component (purple) haze in the intact samples that is cleared away in the permeabilized samples (marked with a *).

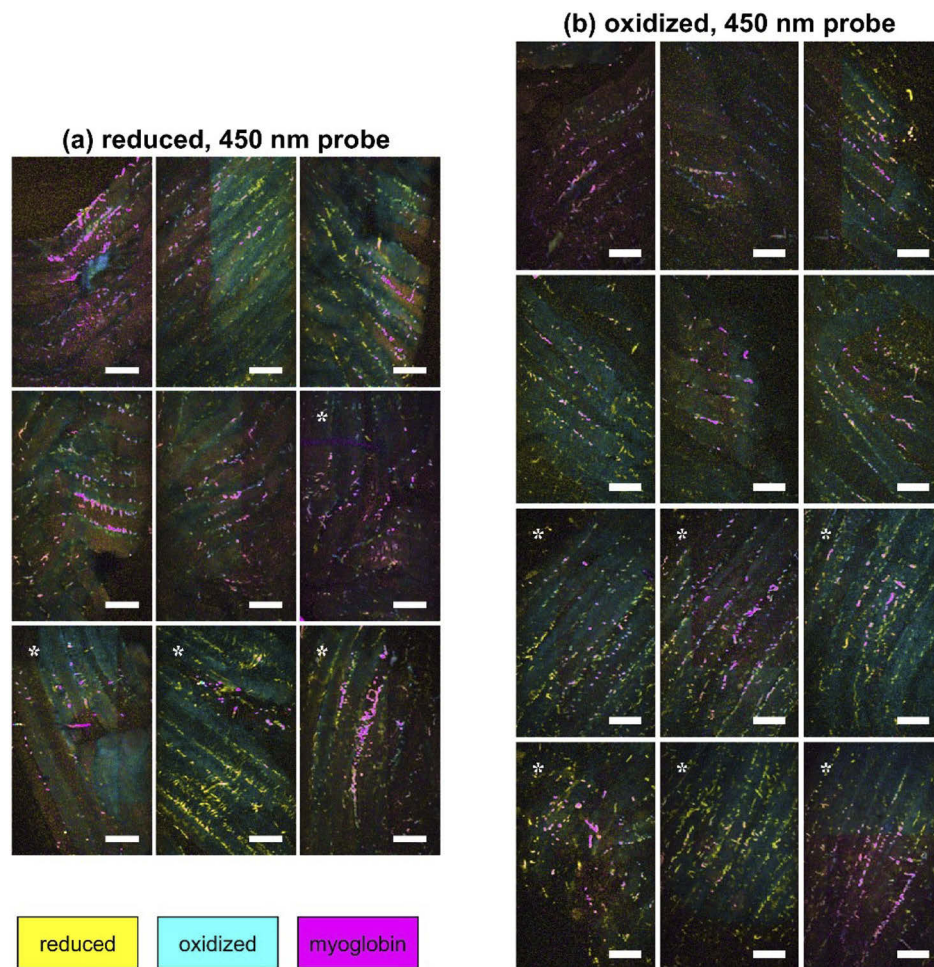


Fig. 5. False-color images for 450 nm probe based on MCR-recovered concentrations of reduced mitochondria (yellow), oxidized mitochondria (cyan), and myoglobin (magenta). (a) Reduced muscle fibers. (b) Oxidized muscle fibers. Asterisk (*) indicates permeabilized fibers. Scale bars 100 μm .

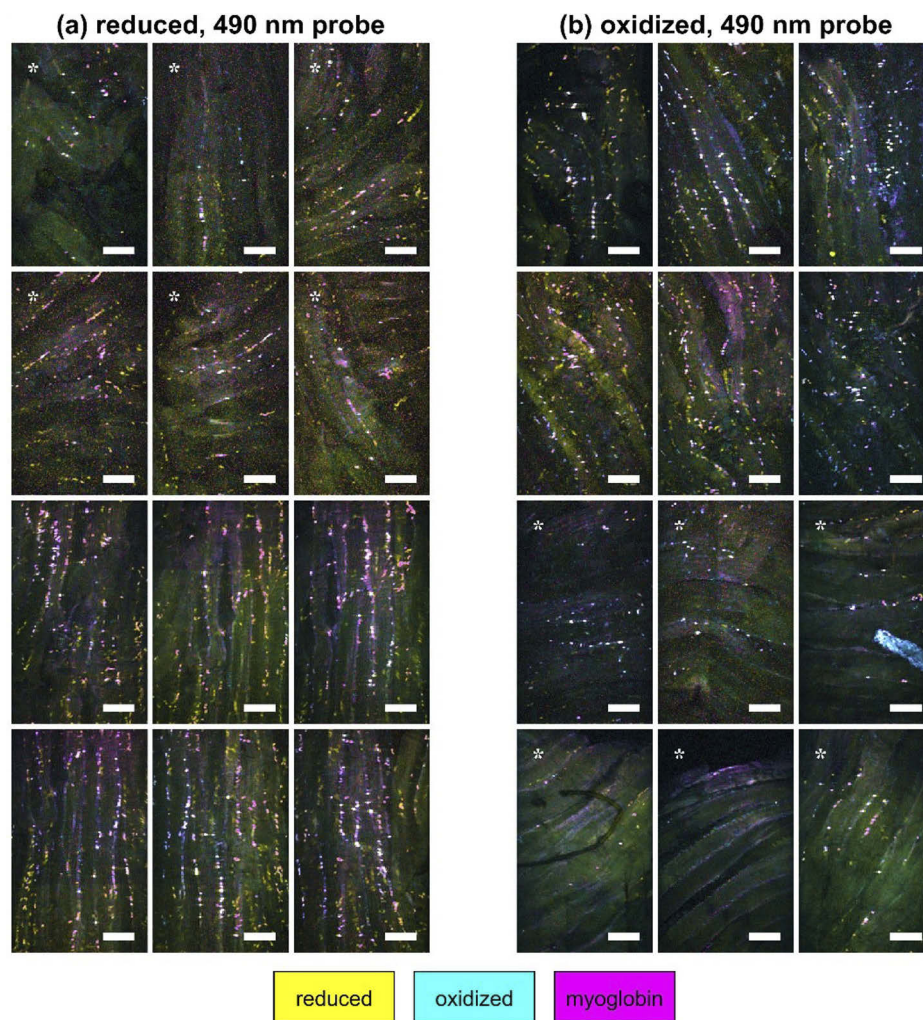


Fig. 6. False-color images for 490 nm probe based on MCR-recovered concentrations of reduced mitochondria (yellow), oxidized mitochondria (cyan), and myoglobin (magenta). (a) Reduced muscle fibers. (b) Oxidized muscle fibers. Asterisk (*) indicates permeabilized fibers. Scale bars 100 μm.

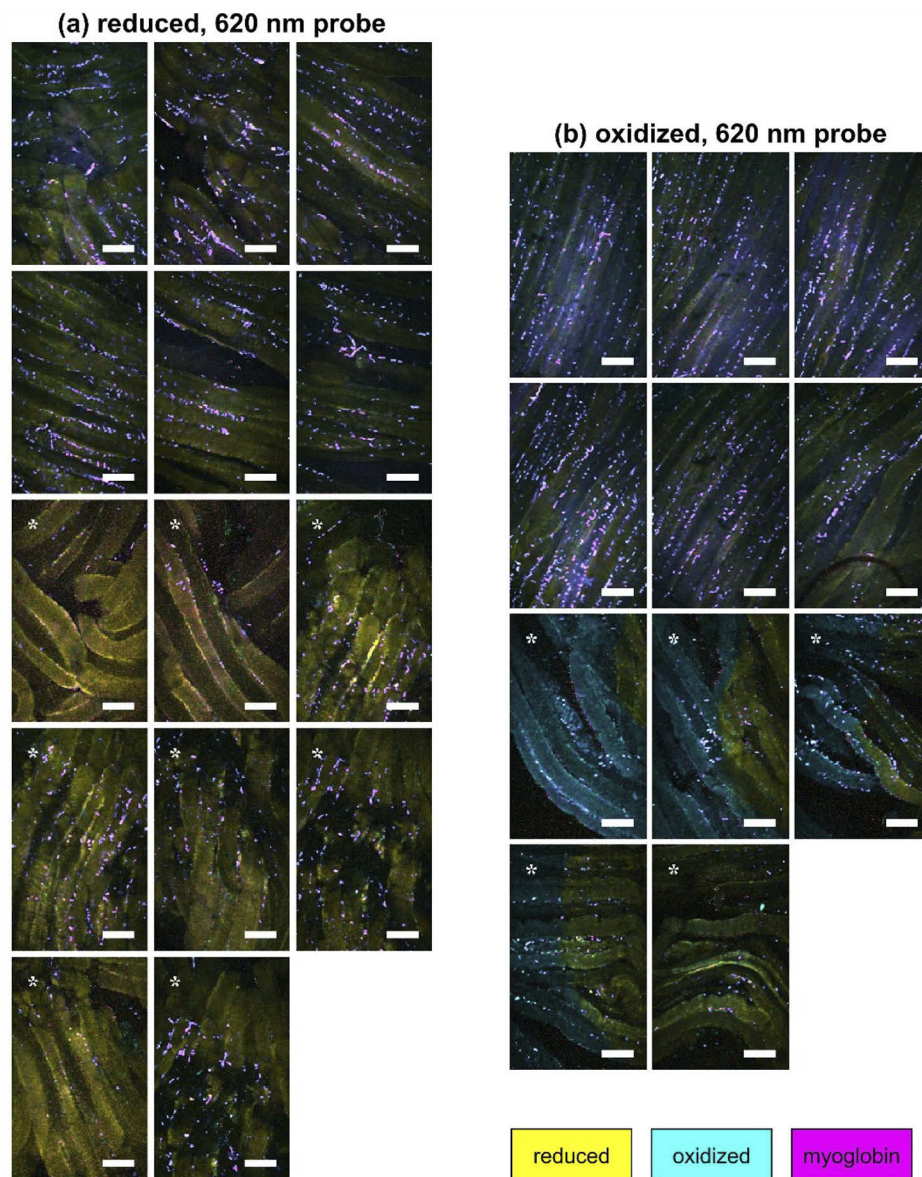


Fig. 7. False-color images for 620 nm probe based on MCR-recovered concentrations of reduced mitochondria (yellow), oxidized mitochondria (cyan), and myoglobin (magenta). (a) Reduced muscle fibers. (b) Oxidized muscle fibers. Asterisk (*) indicates permeabilized fibers. Scale bars 100 μm .

Next, for each pixel, a redox ratio was calculated as the fraction of the reduced component over the sum of reduced and oxidized components,

$$R_i^{\text{redox}} = \frac{M_{i,1}}{M_{i,1} + M_{i,2} + \epsilon}, \quad (4)$$

where $\epsilon = 0.01$ is used to avoid dividing by near-zero values in the case pixels with small signals. For each probe wavelength, the redox ratios were binned into histograms, as shown in Figs. 8(a-c). Again, the 620nm probe provides the clearest redox contrast, judging from the decreased overlap between reduced and oxidized histograms.

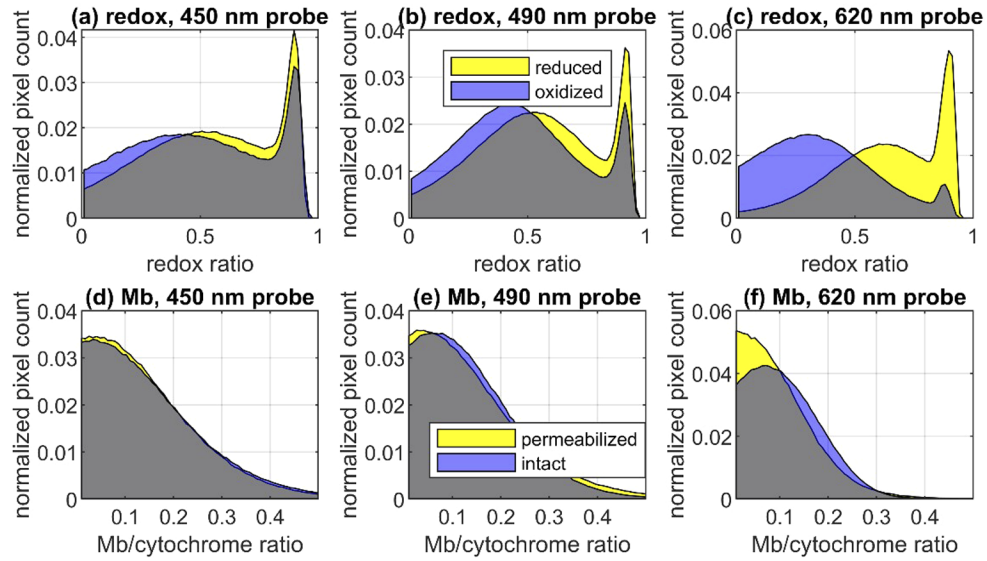


Fig. 8. Redox ratio histograms for (a) 450 nm probe, (b) 490 nm probe, and (c) 620 nm probe. Myoglobin ratio histograms for (d) 450 nm probe, (e) 490 nm probe, and (f) 620 nm probe. Overlap indicated by gray.

Finally, a similar process was used to estimate the myoglobin fraction of each pixel,

$$R_i^{\text{MbO}_2} = \frac{M_{i,3}}{M_{i,1} + M_{i,2} + M_{i,3} + \epsilon}. \quad (5)$$

Histograms of myoglobin fraction are shown in Figs. 8(d-f) comparing intact muscle fibers versus those that had cell membranes permeabilized with saponin. The 450nm probe does not show any difference, but both 490nm and 620nm results indicate that the MbO_2 concentration decreases with permeabilization, as expected.

4. Conclusions

In summary, we have shown visible-wavelength (522nm pump with 450nm, 490nm, or 620nm probe) TAS of mitochondria and TAM of muscle fibers with sub-cellular resolution. For isolated mitochondria, a 450nm probe appears to provide the greatest redox contrast, followed by 620nm. For muscle fibers, however, the 450nm probe shows more photobleaching, significant differences with isolated mitochondria, and loss of redox contrast. On the other hand the 490nm and 620nm probe wavelengths shows closer agreement with isolated mitochondria. Overall, a 620nm probe wavelength reveals the best imaging redox contrast and also the clearest difference

between intact and permeabilized fibers, consistent with the expected loss of myoglobin on permeabilization. We emphasize that the observed mitochondrial redox changes were induced with mitochondria-specific substrates (malate, pyruvate, and succinate) that are incapable of directly changing redox or oxygenation states of other hemeproteins. Further studies involving comparisons with mito- and ER-specific fluorophores and NADH/FAD⁺ will be needed on this point. In addition, studies with cells that lack myoglobin (e.g. hepatocytes, which have high amounts of P450 cytochromes, and fibroblasts which are relatively low in P450) will shed further light on the origin of the visible-wavelength TA signal. In addition, it is unclear at this point which of the respiratory hemes (*a*-, *b*-, or *c*-type cytochromes) are responsible for the observed TA signals, and whether they can be separated by changing pump/probe wavelengths. Nevertheless, the data here show TAM can detect molecular changes in cells in response to the absence or presence of physiological mitochondrial substrates. Further, the characterization of the ultrafast dynamics of respiratory hemeproteins in intact mitochondria within living cells could lead to a better understanding of electron transport, respiratory control, and new diagnostics for mitochondrial dysfunction.

Funding. Boettcher Foundation; Division of Chemical, Bioengineering, Environmental, and Transport Systems (1943595).

Acknowledgments. This material is based upon work supported by the National Science Foundation under Grant No. 1943595. This research was supported in part by funds from the Boettcher Foundation's Webb-Waring Biomedical Research Program.

Disclosures. The authors declare no conflicts of interest.

Data availability. Data underlying the results presented in this paper are not publicly available at this time but may be obtained from the authors upon reasonable request.

References

1. K. Guo, J. Wu, Y. Kong, L. Zhou, W. Li, Y. Fei, J. Ma, and L. Mi, "Label-free and noninvasive method for assessing the metabolic status in type 2 diabetic rats with myocardium diastolic dysfunction," *Biomed. Opt. Express* **12**, 480 (2021).
2. S. Manioglou, M. Atis, M. Aas, A. Kiraz, and H. Bayraktar, "Direct conversion of Cytochrome c spectral shifts to fluorescence using photochromic FRET," *Chem. Commun.* **50**(82), 12333–12336 (2014).
3. M. Okada, N. I. Smith, A. F. Palonpon, H. Endo, S. Kawata, M. Sodeoka, and K. Fujita, "Label-free Raman observation of cytochrome c dynamics during apoptosis," *Proc. Natl. Acad. Sci.* **109**(1), 28–32 (2012).
4. N. Yasuda, S. Takeshita, and Shigeto, "Inhomogeneous Molecular Distributions and Cytochrome Types and Redox States in Fungal Cells Revealed by Raman Hyperspectral Imaging Using Multivariate Curve Resolution-Alternating Least Squares," *Anal. Chem.* **91**(19), 12501–12508 (2019).
5. N. A. Brazhe, M. Treiman, A. R. Brazhe, N. L. Find, G. V. Maksimov, and O. V. Sosnovtseva, "Mapping of Redox State of Mitochondrial Cytochromes in Live Cardiomyocytes Using Raman Microspectroscopy," *PLoS One* **7**(9), e41990 (2012).
6. T. Morimoto, L. da Chiu, H. Kanda, H. Kawagoe, T. Ozawa, M. Nakamura, K. Nishida, K. Fujita, and T. Fujikado, "Using redox-sensitive mitochondrial cytochrome Raman bands for label-free detection of mitochondrial dysfunction," *Analyst* **144**(8), 2531–2540 (2019).
7. S. Lu, W. Min, S. Chong, G. R. Holtom, and X. S. Xie, "Label-free imaging of heme proteins with two-photon excited photothermal lens microscopy," *Appl. Phys. Lett.* **96**(11), 113701 (2010).
8. C. Zhang, Y. S. Zhang, D.-K. Yao, Y. Xia, and L. V. Wang, "Label-free photoacoustic microscopy of cytochromes," *J. Biomed. Opt.* **18**(2), 020504 (2013).
9. M. C. Fischer, J. W. Wilson, F. E. Robles, and W. S. Warren, "Invited Review Article: Pump-probe microscopy," *Rev. Sci. Instrum.* **87**(3), 031101 (2016).
10. Y. Zhu and J. X. Cheng, "Transient absorption microscopy: Technological innovations and applications in materials science and life science," *J. Chem. Phys.* **152**(2), 020901 (2020).
11. N. F. Scherer, J. L. Knee, D. D. Smith, A. H. Zewail, and A. Amos, *LETTERS Femtosecond Photofragment Spectroscopy: The Reaction ICN-CN + I (n.d.)*, Vol. 5.
12. O. Bräm, C. Consani, A. Cannizzo, and M. Chergui, "Femtosecond UV studies of the electronic relaxation processes in Cytochrome c," *J. Phys. Chem. B* **115**(46), 13723–13730 (2011).
13. C. Consani, O. Bräm, F. van Mourik, A. Cannizzo, and M. Chergui, "Energy transfer and relaxation mechanisms in Cytochrome c," *Chem. Phys.* **396**, 108–115 (2012).
14. C. Zang, J. A. Stevens, J. J. Link, L. Guo, L. Wang, and D. Zhong, "Ultrafast proteinquake dynamics in cytochrome c," *J. Am. Chem. Soc.* **131**(8), 2846–2852 (2009).

15. P. A. Anfinrud, C. Han, and R. M. Hochstrasser, "Direct observations of ligand dynamics in hemoglobin by subpicosecond infrared spectroscopy," *Proc. Natl. Acad. Sci.* **86**(21), 8387–8391 (1989).
16. E. R. Henry, J. H. Sommer, J. Hofrichter, W. A. Eaton, and M. Gellert, "Geminate recombination of carbon monoxide to myoglobin," *J. Mol. Biol.* **166**(3), 443–451 (1983).
17. P.-T. Dong, H. Lin, K.-C. Huang, and J.-X. Cheng, "Label-free quantitation of glycated hemoglobin in single red blood cells by transient absorption microscopy and phasor analysis," *Sci. Adv.* **5**, 5 (2019).
18. D. Fu, T. Ye, T. E. Matthews, B. J. Chen, G. Yurtserver, and W. S. Warren, "High-resolution in vivo imaging of blood vessels without labeling," *Opt. Lett.* **32**(18), 2641–2643 (2007).
19. D. Fu, T. E. Matthews, T. Ye, I. R. Piletic, and W. S. Warren, "Label-free in vivo optical imaging of microvasculature and oxygenation level," *J. Biomed. Opt.* **13**(4), 040503 (2008).
20. A. T. Francis, K. Berry, E. C. Thomas, A. H. Hill, and D. Fu, "In vitro quantification of single red blood cell oxygen saturation by femtosecond transient absorption microscopy," *J. Phys. Chem. Lett.* **10**(12), 3312–3317 (2019).
21. A. T. Francis, M. J. Shears, S. C. Murphy, and D. Fu, "Direct quantification of single red blood cell hemoglobin concentration with multiphoton microscopy," *Anal. Chem.* **92**(18), 12235–12241 (2020).
22. A. J. Chen, X. Yuan, J. Li, P. Dong, I. Hamza, and J. X. Cheng, "Label-free imaging of heme dynamics in living organisms by transient absorption microscopy," *Anal. Chem.* **90**(5), 3395–3401 (2018).
23. S. R. Domingue, R. A. Bartels, A. J. Chicco, and J. W. Wilson, "Transient absorption imaging of hemes with 2-color, independently tunable visible-wavelength ultrafast source," *Biomed. Opt. Express* **8**(6), 2807–2821 (2017).
24. E. Wang, K. S. Specht, A. J. Chicco, and J. W. Wilson, "High-repetition-rate transient absorption spectroscopy of respiratory supercomplexes," *J. Phys. Chem. B* **126**(7), 1404–1412 (2022).
25. S. R. Domingue, A. J. Chicco, R. A. Bartels, and J. W. Wilson, "Pump-probe microscopy of respiratory chain pigments: towards non-fluorescent label-free metabolic imaging," in *Proc. SPIE 10069, Multiphoton Microscopy in the Biomedical Sciences XVII*, A. Periasamy, P. T. C. So, K. König, and X. S. Xie, eds. (SPIE, 2017), Vol. 10069, p. 100691P.
26. J. D'Errico, "Surface Fitting using gridfit," MATLAB Central File Exchange, 2022, <https://www.mathworks.com/matlabcentral/fileexchange/8998-surface-fitting-using-gridfit>.
27. C. Greene, "gridbin," Github, 2021, <https://github.com/chadagreene/gridbin>.
28. M. Talone, A. Bazzarelli, F. Schirato, D. dello Vicario, E. Viola, M. Jacchetti, M. T. Bregonzio, G. Raimondi, D. Cerullo, and Polli, "Phototoxicity induced in living HeLa cells by focused femtosecond laser pulses: a data-driven approach," *Biomed. Opt. Express* **12**(12), 7886 (2021).
29. National Research Council, *Guide for the Care and Use of Laboratory Animals: Eighth Edition* (The National Academies Press, 2011).
30. L. C. Li Puma, M. Hedges, J. M. Heckman, A. B. Mathias, M. R. Engstrom, A. B. Brown, and A. J. Chicco, "Experimental oxygen concentration influences rates of mitochondrial hydrogen peroxide release from cardiac and skeletal muscle preparations," *Am. J. Physiol. Regul. Integr. Comp. Physiol.* **318**(5), R972–R980 (2020).
31. D. Pesta and E. Gnaiger, "High-resolution respirometry: OXPHOS protocols for human cells and permeabilized fibers from small biopsies of human muscle," in *Mitochondrial Bioenergetics: Methods and Protocols*, C. M. Palmeira and A. J. Moreno, eds. (Humana Press, 2012), pp. 25–58.
32. B. Glancy, L. M. Hartnell, D. Malide, Z.-X. Yu, C. A. Combs, P. S. Connelly, S. Subramaniam, and R. S. Balaban, "Mitochondrial reticulum for cellular energy distribution in muscle," *Nature* **523**(7562), 617–620 (2015).
33. R. M. Barbosa, R. M. Santos, C. Pereira, C. F. Lourenço, A. J. Lopes Jesus, C. L. Pereira, C. F. Marques, B. S. Rocha, N. R. Ferreira, A. Ledo, and J. Laranjinha, *Preparation, Standardization and Measurement of Nitric Oxide Solutions Nitrate-Nitrite-NO Pathway View Project Living with Intention, Fullness and Engagement with Inflammatory Bowel Disease: The Impact of a Group Intervention and an ICT-Based Transcultural Intervention on Physical and Mental Health View Project GLOBAL JOURNAL OF ANALYTICAL CHEMISTRY Preparation, Standardization and Measurement of Nitric Oxide Solutions* (2011), Vol. 2.
34. R. Tauler, A. Izquierdo-Ridorsa, and E. Casassas, *Simultaneous Analysis of Several Spectroscopic Titrations with Self-Modelling Curve Resolution* (1993), Vol. 18.
35. A. de Juan, J. Jaumot, and R. Tauler, "Multivariate Curve Resolution (MCR). Solving the mixture analysis problem," *Anal. Methods* **6**(14), 4964–4976 (2014).
36. F. E. Robles, J. W. Wilson, M. C. Fischer, and W. S. Warren, "Phasor analysis for nonlinear pump-probe microscopy," *Opt. Express* **20**, 17082–17092 (2016).
37. A. Thompson, F. E. Robles, J. W. Wilson, S. Deb, R. Calderbank, and W. S. Warren, "Dual-wavelength pump-probe microscopy analysis of melanin composition," *Sci. Rep.* **6**(1), 36871 (2016).
38. D. Zhang, P. Wang, M. N. Slipchenko, D. Ben-Amotz, A. M. Weiner, and J.-X. Cheng, "Quantitative vibrational imaging by hyperspectral stimulated Raman scattering microscopy and multivariate curve resolution analysis," *Anal. Chem.* **85**(1), 98–106 (2013).
39. I. J. Pence, B. A. Kuzma, M. Brinkmann, T. Hellwig, and C. L. Evans, "Multi-window sparse spectral sampling stimulated Raman scattering microscopy," *Biomed. Opt. Express* **12**(10), 6095–6114 (2021).
40. A. E. Yagle, "Regularized Matrix Computations," <https://web.eecs.umich.edu/~acy/recent/regular.pdf>.